JACS
JOURNAL OF THE AMERICAN CHEMICAL SOCIETY
Communication
pubs.acs.org/JACS

Surface Structure-Dependent Molecular Oxygen Activation of BiOCl Single-Crystalline Nanosheets

Kun Zhao,[†] Lizhi Zhang,*[,†] Jiajun Wang,[‡] Qunxiang Li,[‡] Weiwei He,[§] and Jun Jie Yin[§]

[†]Key Laboratory of Pesticide & Chemical Biology of Ministry of Education, Institute of Environmental Chemistry, College of Chemistry, Central China Normal University, Wuhan 430079, P. R. China

[‡]Hefei National Laboratory for Physical Sciences at the Microscale, University of Science and Technology of China, Hefei 230026, Anhui, P. R. China

[§]Center for Food Safety and Applied Nutrition, Food and Drug Administration, College Park, Maryland 20740, United States

Supporting Information

ABSTRACT: We demonstrate that BiOCl single-crystalline nanosheets possess surface structure-dependent molecular oxygen activation properties under UV light. The (001) surface of BiOCl prefers to reduce O_2 to $\cdot O_2^-$ through one-electron transfer, while the (010) surface favors the formation of O_2^{2-} via two-electron transfer, which is cogoverned by the surface atom exposure and the situ generated oxygen vacancy characteristics of the (001) and (010) surfaces under UV light irradiation.

Molecular oxygen is the most green and low-cost oxidant. Unfortunately, it cannot oxidize most organic pollutants under ambient conditions because of spin forbidden reactions.[1] Photocatalysis activates molecular oxygen when photogenerated electrons on the surface of semiconductors reduce oxygen. This not only inhibits the recombination of photogenerated electron−hole pairs but also produces reactive oxygen species (ROS) like $\cdot O_2^-$, H_2O_2, and $\cdot OH$.[2] Molecular oxygen activation during photocatalysis generally proceeds via one- or two-electron reduction, depending on the first step of sequential reactions on the surface of semiconductors,[3] so it is extremely important to understand the interaction between molecular oxygen and semiconductor surfaces, especially how the surface properties of semiconductors control the first step of the molecular oxygen activation process.

However, our knowledge of surface-dependent molecular oxygen activation is mostly limited to TiO_2 photocatalysis. For example, researchers reported that O_2 that was adsorbed onto the oxygen vacancies of rutile (110) or anatase (101) surfaces could convert into either $\cdot O_2^-$ or O_2^{2-}, depending on the amount of O_2 adsorbed at low temperatures.[2a,e,g,4] Recently, Zhao's group reported peroxide states of O_2 bound to anatase TiO_2 during the photocatalytic oxidation of alcohols and found photoinduced electron-activated dioxygen could react with alcohols using different reaction pathways on anatase {001} and {101} facets because of their surface structures.[3a,5]

Bismuth oxyhalides have attracted more and more attention in the field of photocatalysis because of their interesting, structure-dependent photocatalytic performance that arises from their layered structure interleaved with $[Bi_2O_2]$ slabs and double halogen atoms slabs.[6] Their layered structure can not only inhibit the recombination of photogenerated charge carriers due to internal electric fields formed between the $[Bi_2O_2]$ and halogen layers but also can reduce the surface trapping of photogenerated carriers because the low-dangling bonds produced by the covalently bonded layers result in fewer surface defects. We recently reported that the variation of pH value from 1 to 6 could change the facet exposure of BiOCl (BOC) single-crystalline nanosheets from {001} to {010}, and we indicated this by calling them BOC-001 and BOC-010. The BOC-001 nanosheets exhibited higher activity during direct semiconductor photoexcitation pollutant degradation under UV light because of a cooperative effect between the surface atomic structure and suitable internal electric fields. In contrast, BOC-010 nanosheets exhibited higher activity during indirect dye photosensitization degradation under visible light owing to their larger surface area and open channel characteristics.[7] However, the first step of the interaction between molecular oxygen and distinct surfaces during BOC photocatalysis is still unknown.

Here, we demonstrate the surface-dependent molecular oxygen activation properties of BOC single-crystalline nanosheets by computing and monitoring ROS generation in BOCs with exposed {001} and {010} facets. We also systematically investigate the influence of surface atom exposure and in situ generated oxygen vacancies on molecular oxygen activation with different BOC facets.

It is widely accepted that the {001} facets of BOC are highly oxygen dense.[8] However, the model of definite (001) surface atom termination related to surface exposure is still controversial because all three kinds of atom terminations (O, Bi, and Cl terminations) are demonstrated by its layered structure but have not been verified using the thermodynamic surface energy (γ) associated with practical environment of surface exposure. Therefore, our first step was to compare the thermodynamic stability of O and Bi terminations on (001) through γ computation, leaving out the nonbonding van der Waals Cl termination. We found that the surface energy ($\gamma_{001\text{-Bi}}$) of Bi terminated (001) surfaces (001-Bi) increased with the upshift of the chemical potential of oxygen (μ_O). This indicates that 001-Bi is unstable in O-rich environments and may recombine with oxygen because of the high bonding energy (343 kJ mol^{-1}) of Bi−O.[9] In contrast, the surface energy ($\gamma_{001\text{-O}}$, cal. 2.42 J m^{-2}) of

Received: September 8, 2013
Published: October 11, 2013

   dx.doi.org/10.1021/ja4092903 | J. Am. Chem. Soc. 2013, 135, 15750−15753

O-terminated (001) surfaces (001-O) was much smaller in O-rich environments but still larger than the surface energy (γ_{010}, cal. 0.51 J m^{-2}) of (010) constructed by [BiOCl] units with stoichiometry and no formal charge on each atomic layer (Figure 1b,c).

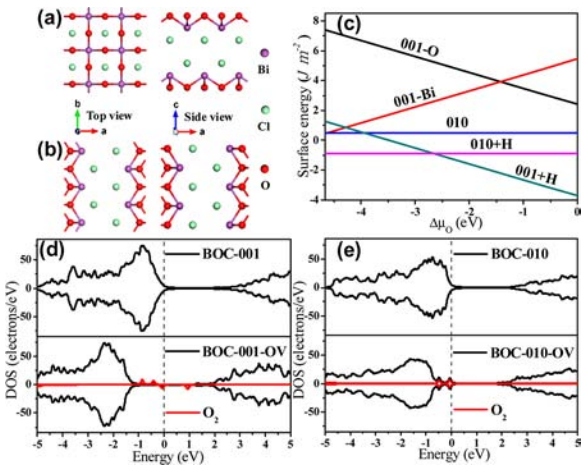

Figure 1. The structure of (a) (001) and (b) (010) surfaces. (c) The comparison of the calculated surface energy. (d,e) DOS for clean surfaces and surfaces with oxygen vacancies and O_2 adsorption. The positive and negative *y* values represent majority and minority spin states, respectively. The vertical dashed line shows VBM.

We then calculated the models of hydrogen adsorption on (001) surface oxygen atoms, taking into account the abundant protons in acid solution (pH = 1) during the synthesis of BOC-001 and the strong H−O bonding energy of 428 kJ mol^{-1}.[9] As expected, the surface energy (γ_{001+H}, cal. −3.71 J m^{-2}) of the hydrogen-adsorbed (001) surface became significantly lower than the that of the original surface (Figure 1c). Meanwhile, the magnetic moment of the (001) slab decreased from 26.62 to 0 μ_B after hydrogen adsorption because the dangling bonds of surface oxygen atoms were compensated by adsorbed hydrogen (Table S1 and Figure S1), suggesting that the hydrogen-adsorbed (001) slab might be the real situation. However, hydrogen adsorption resulted in the increase of the magnetic moment of the (010) slab from 0 to 5.01 μ_B because the self-compensated charge of the stoichiometric [BiOCl] units in the (010) slab was out of equilibrium after hydrogen adsorption, despite its substantial negative surface energy. This indicated that the hydrogen-adsorbed (010) slab was not as stable as the original one. We therefore concluded that the high-energy {001} facets of BOCs are stabilized by protons bonded to surface oxygen atoms, which explains why BiOCl single-crystalline nanosheets with exposed {001} facets of high surface energy could be obtained at pH 1 in our previous study.[7]

On the basis of the above analysis, we used the models of hydrogen-adsorbed O-terminated (001) and clean (010) slabs to investigate oxygen activation in the (001) and (010) facets of BOC. We first optimized the geometric structure of O_2 adsorbed on a perfect (001) surface but found the height of adsorption reached 3.21 Å, which ruled out the possibility of chemisorption. However, O_2 can be adsorbed on oxygen vacancies (OV) through combining with two nearest Bi atoms in the sublayers to form an end-on structure on (001) surface. The O−O bond length in the two structures was activated to 1.32 Å, which is close to that of $\cdot O_2^-$ (1.26 Å). The adsorption of O_2 on the clean (010) surface was theoretically impossible because the adsorption layer was as high as 2.46 Å. O_2 can also interact with the OV of the (010) surface by combining with two nearest Bi atoms in outerlayer and one next nearest Bi atom in sublayer to form a complex bridge-on structure. Interestingly, the O−O bond length of O_2 bound to the OV of the (010) surface was weakened to 1.46 Å, close to the bond lengths of O_2^{2-} (1.49 Å) and H_2O_2 (1.48 Å). We therefore hypothesized that the different O_2 adsorption structures on (001) and (010) surfaces, which are predetermined by OV, might result in facet-dependent oxygen activation on BiOCl single-crystalline nanosheets.

To confirm this opinion, we calculated the density of states (DOS) to analyze the electron interaction between BOC surfaces and O_2. As illustrated in Figure 1c,d, pure BOC surfaces were spin paired with symmetric majority and minority states of Bi atoms. After OV generation and O_2 adsorption, the spin states of the BOC surfaces changed to match the different oxygen states. On the (001) surface, the previous symmetric majority and minority states of Bi atoms at the valence-band maximum (VBM) broke up to provide donor sites for O_2 (Figures 2a and

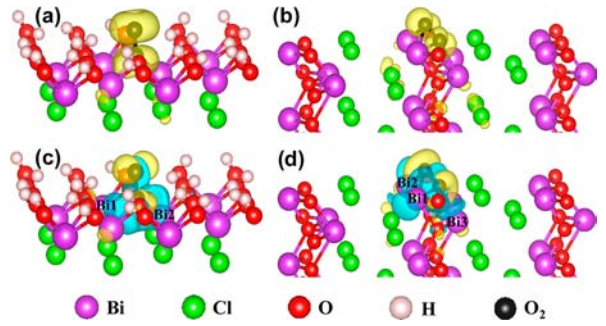

Figure 2. The VBM charge density in the energy range (a) from −1.2 to 0 eV for O_2-adsorbed BOC-001 and (b) from −0.8 to 0 eV for O_2-adsorbed BOC-010. The charge density difference of the (c) O_2-adsorbed BOC-001 and (d) O_2-adsorbed BOC-010. The yellow and blue isosurfaces represent charge accumulation and depletion in the space, respectively. The adsorbed O_2 were highlighted with black color. The charge density that is changed in whole processes can only be located in the three outer atomic layers. For clarity, the symmetric parts of the optimized slabs at the bottom are not shown. The isovalue is 0.002 au.

S2). Nevertheless, these new Bi atom spin states facilitated the formation of O 2p states with two occupied majority, one occupied minority, and one empty minority states. The resulting O_2 had a magnetic moment of 0.81 μ_B, suggesting that the activated dioxygen was in a −1 reduced valence state of low-spin π^{*3}, matching the electron configuration of $\cdot O_2^-$ very well. In contrast, the spin states of BOC-010 reorganized from all the surface atom orbitals though maintaining symmetric majority and minority states and produced different O_2 2p states from that of $\cdot O_2^-$ (Figure S2). The resulting spin of O_2, which is composed of two symmetrically occupied majority and minority states without magnetic moment, is similar to the electronic configuration of O_2^{2-} (π^{*4}). These electronic structure calculation results not only verify the aforementioned different bond activations of O_2 on BOC-001 and BOC-010 surfaces but also imply distinct molecular oxygen activation processes on BOC-001 and BOC-010 surfaces.

To further understand the electron-transfer pathway of molecular oxygen activation processes on BOC surfaces, we employed the charge density difference, in conjunction with the

dx.doi.org/10.1021/ja4092903 | J. Am. Chem. Soc. 2013, 135, 15750−15753

Bader charge and charge density,[10] to trace the electron behavior. The exchange and transfer of electrons took place between the OV-connected surface Bi atoms (Bi1, Bi2 and Bi3) and O_2 molecules (Figure 2c,d). On the (001) surface, the reduction accompanied by the generation of OV under UV light produced excess electrons. These electrons delocalized around the neighboring Bi and O atoms, accumulated mainly at the nearest Bi1 and Bi2 atoms (Figure S1c) and then transferred to the O_2 π^* orbital as soon as O_2 was adsorbed onto the OV. The electron transfer depleted the charges of the Bi atoms, which is in accord with the calculated one-electron transfer in the Bader charge (Table S1). As for the (010) surface, the excess electrons induced by the generation of OV also gathered at the adjoining Bi1, Bi2, and Bi3 atoms with slight spreading to the adjacent O and Cl atoms (Figure S1f). When O_2 adsorbed onto the OV, these electrons transferred from the Bi1, Bi2, and Bi3 atoms to O_2 to generate a new electron configuration of O_2 through the two-electron transfer of the Bader charge. Therefore, various bonding configurations of surface Bi atoms and O_2 induced different electron transfers and facet-dependent molecular oxygen activation processes in BOCs.

To confirm the theoretical calculation results on molecular oxygen activation, we monitored ROS generation in BOC-001 and BOC-010 under UV light by using electron spin resonance (ESR) techniques, the most effective analytical methods to detect radicals, with 5-*tert*-butoxycarbonyl 5-methyl-1-pyrroline *N*-oxide (BMPO) as a spin-trapping agent for both $\cdot O_2^-$ and ·OH.[11] No signal could be observed in the dark, which indicated that there was no chemisorption of O_2 on clean surfaces (Figure 3a,b). This finding supported the calculation results.

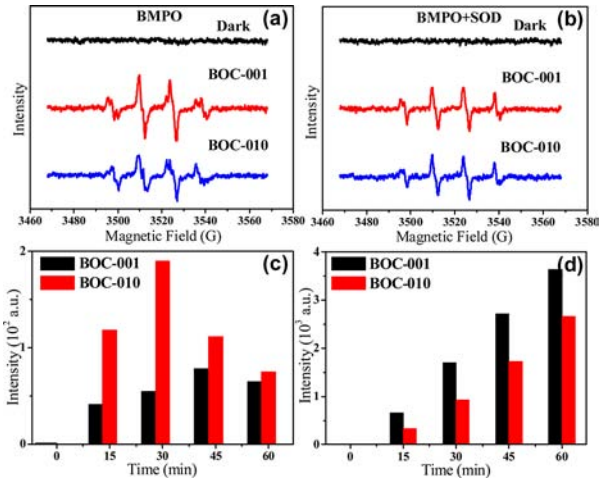

Figure 3. ESR spectra of active oxygen radicals generated during BOC-001 and BOC-010 photocatalysis (a) before and (b) after SOD addition. (c) The amount of H_2O_2 and (d) ·OH from the reduction of O_2 by photogenerated electrons over BOC-001 and BOC-010 surfaces under UV light irradiation.

After UV irradiation for 3 min, a strong four-line ESR spectrum was observed with the relative intensities of 1:2:2:1 and splitting parameters of $a^N = 13.56$, $a^\beta_H = 12.30$, $a^\gamma_H = 0.66$ over both BOC-001 and BOC-010, which is the characteristic spectrum for BMPO/·OH adduct.[11] The superoxide was also captured to form BMPO/$\cdot O_2^-$ adduct having four-line spectrum with relative intensities of 1:1:1:1 and hyperfine splitting parameters of a^N = 13.56, a^β_H = 12.10, which is overlapping with BMPO/·OH. To verify whether the ESR signal in part involved with superoxide, we added superoxide dismutase (SOD) capable of converting $\cdot O_2^-$ into H_2O_2 through disproportionation. Intriguingly, after SOD was added, the ESR signal intensity was notably decreased but not much both for BOC-001 and BOC-010 samples. These indicated both ·OH and $\cdot O_2^-$ were generated from irradiated BOC but ·OH dominated, leading to the unclear characteristic of ESR signal for $\cdot O_2^-$. Nevertheless, the reduction of ESR peak intensity after the same addition of SOD was much more significant over BOC-001 than over BOC-010, reflecting that the amount of $\cdot O_2^-$ generated by BOC-001 was much greater than that generated by BOC-010. Obviously, these ESR results are consistent with the theoretical calculations.

Because both $\cdot O_2^-$ and O_2^{2-} could transform to H_2O_2 via $\cdot O_2^- + e + 2H^+ \rightarrow H_2O_2$ and $O_2^{2-} + 2H^+ \rightarrow H_2O_2$, respectively,[3a,12] we employed the *p*-hydroxyphenylacetic acid photoluminescence method to determine the amount of H_2O_2 generated from BOC samples with different exposed surfaces and further check the molecular oxygen activation pathways.[13] Since H_2O_2 could also be generated via photogenerated holes of BOC oxidation, we utilized the amount of H_2O_2 by subtracting the amount of H_2O_2 produced in air with that produced in Ar gas to estimate the H_2O_2 generation via molecular oxygen reduced by photogenerated electrons on the (001) and (010) facets of BOCs. We found that much less H_2O_2 was generated from BOC-001 than BOC-010 (Figure 3c). Since the other species were the same in the $\cdot O_2^-$ and O_2^{2-} transformation, we think that the H_2O_2 generation might be rate limited by photogenerated electrons from the BOC-001 substrate and that H_2O_2 is formed by two sequential one-electron reduction processes ($O_2 \rightarrow \cdot O_2^- \rightarrow H_2O_2$) on BOC-001 surface, while one two-electron reduction pathway ($O_2 \rightarrow H_2O_2$) would govern the production of H_2O_2 on BOC-010 surface. These different H_2O_2 generation pathways are consistent with DFT calculations and ESR results and verify the facet-dependent molecular oxygen activation processes on BOC surfaces.

During BiOCl photocatalysis, H_2O_2 could be decomposed to ·OH by either photogenerated electrons or UV irradiation, which was confirmed by ESR analysis. We further measured the amount of ·OH generated over BOC-001 and BOC-010 under UV light with the terephthalic acid photoluminescence method.[14] If the decomposition rates of H_2O_2 into ·OH under UV light are the same during BOC-001 and BOC-010 photocatalysis, more ·OH should be generated from BOC-010 because more H_2O_2 was detected. Unexpectedly, both the generation rate and the total amount of ·OH were higher during BOC-001 photocatalysis than BOC-010 photocatalysis (Figure 3d), suggesting that there might be more or faster ways to generate ·OH from BOC-001. The larger amount of ·OH generated from BOC-001 allowed BOC-001 to degrade colorless salicylic acid more rapidly than BOC-010 by direct semiconductor photoexcitation under UV light (Figure S3).

The generation of OV on BOC-001 under UV light irradiation was validated by ESR and X-ray photoelectron spectroscopy,[8,15] but the formation of OV on BOC-010 has not been reported yet. We utilized Raman spectra to check OV generation on BOC-001 and BOC-010 surfaces under UV irradiation (Figure S4). We illuminated BOC-001 and BOC-010 in deionized water with UV light for 2.5 h to produce two samples with OV that we called BOC-001-UV and BOC-010-UV. As expected, the B_{1g} band at about 396 cm^{-1} ascribed to the motion of the oxygen atoms disappeared in the Raman spectra of BOC-001-UV, and new bands emerged at 69 and 94 cm^{-1}. These two new bands could be assigned to first-order vibration modes E_g and A_{1g} of Bi metal,[16]

dx.doi.org/10.1021/ja4092903 | J. Am. Chem. Soc. 2013, 135, 15750−15753

confirming the reduction of Bi^{3+} due to the formation of OV after UV irradiation. The Raman spectra of BOC-010-UV were similar to those of BOC-001-UV: the band of oxygen atoms at 396 cm^{-1} disappeared and new bands at 70 and 95 cm^{-1} appeared, verifying the formation of OV on BOC-010 under UV light. The stability of two BOCs with OV was checked by X-ray diffraction analysis, which revealed that the UV-induced generation of OV did not change the crystal structure of the samples and the BOC samples with OV possessed high stability (Figure S5).

On the basis of our theoretical calculations and experimental results, we propose possible facet-dependent molecular oxygen activation pathways on BiOCl single-crystalline nanosheets under UV light (Figure 4). First, UV light induces the formation

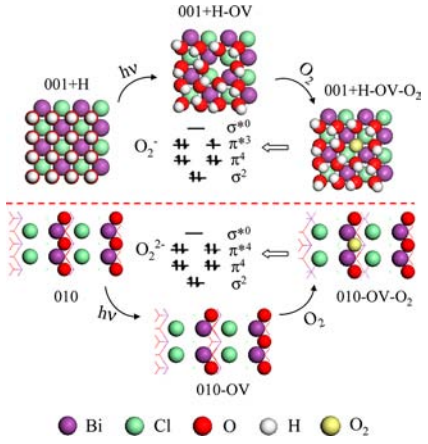

Figure 4. Proposed molecular oxygen activation processes on BOC-001 and BOC-010 surfaces.

of different OV structures on BOC-001 and BOC-010 surfaces because of their different surface atomic structure. Molecular oxygen would then be adsorbed onto the OV site of BOC-001 surface and form an end-on structure with the two nearest sublayer Bi atoms that extracts one electron from redistributed surface charges to generate $\cdot O_2^-$. On BOC-010 surface, O_2 adsorbed on the OV site combines three neighboring Bi atoms to form a complex bridge-on configuration that promotes the simultaneous transfer of two electrons to adsorbed O_2 and generates O_2^{2-} species.

In conclusion, we have demonstrated the surface structure-dependent molecular oxygen activation properties of BiOCl single-crystalline nanosheets under UV light. The (001) surface of BiOCl prefers to reduce O_2 to $\cdot O_2^-$ through one-electron transfer, while the (010) surface favors the formation of O_2^{2-} via two-electron transfer, which is cogoverned by the different surface atomic structure and the in situ generated oxygen vacancy characteristics of (001) and (010) surface under UV light irradiation. These findings will deepen our understanding of molecular oxygen activation on surface structures in photocatalytic reactions and allow us to sensitively manipulate the reaction processes.

■ ASSOCIATED CONTENT

Supporting Information

Additional descriptions, figures, and tables. These materials are available free of charge via the Internet at http://pubs.acs.org.

■ AUTHOR INFORMATION

Corresponding Author

zhanglz@mail.ccnu.edu.cn

Notes

The authors declare no competing financial interest.

■ ACKNOWLEDGMENTS

This work was supported by the National Basic Research Program of China (973 Program) (grants 2013CB632402 and 2011CB921404) and the National Science Foundation of China (grants 21073069, 91023010, and 21177048) and was partially supported by a regulatory science grant under the FDA Nanotechnology CORES Program and by the Office of Cosmetics and Colors, CFSAN/FDA (W.H and J.Y). We would like to thank Barbara Berman for the English writing improvement.

■ REFERENCES

(1) (a) Metz, M.; Solomon, E. I. *J. Am. Chem. Soc.* **2001**, *123*, 4938. (b) Minaev, B. F.; Int, J. *Quantum Chem.* **1980**, *17*, 367.

(2) (a) Linsebigler, A. L.; Lu, G. Q.; Yates, J. T., Jr. *Chem. Rev.* **1995**, *95*, 735. (b) Li, Y.; Zhang, W.; Niu, J. F.; Chen, Y. S. *ACS Nano* **2012**, *6*, 5164. (c) Henderson, M. A.; Lyubinetsky, I. *Chem. Rev.* **2013**, *113*, 4428. (d) Wahlstrom, E.; Vestergaard, E. K.; Schaub, R.; Ronnau, A.; Vestergaard, M.; Lagsgaard, E.; Stensgaard, I.; Besenbacher, F. *Science* **2004**, *303*, 511. (e) Petrik, N. G.; Kimmel, G. A. *J. Phys. Chem. Lett.* **2011**, *2*, 2790. (f) Wang, Z. T.; Du, Y. G.; Dohnalek, Z.; Lyubinetsky, I. *J. Phys. Chem. Lett.* **2010**, *1*, 3524. (g) Aschauer, U.; Chen, J.; Selloni, A. *Phys. Chem. Chem. Phys.* **2010**, *12*, 12956.

(3) (a) Zhao, Y. B.; Ma, W. H.; Li, Y.; Ji, H. W.; Chen, C. C.; Zhu, H. Y.; Zhao, J. C. *Angew. Chem., Int. Ed.* **2012**, *51*, 3188. (b) Khachatryan, L.; Vejerano, E.; Lomnicki, S.; Dellinger, B. *Environ. Sci. Technol.* **2011**, *45*, 8559.

(4) (a) Tan, S. J.; Ji, Y. F.; Zhao, Y.; Zhao, A. D.; Wang, B.; Yang, J. L.; Hou, J. G. *J. Am. Chem. Soc.* **2011**, *133*, 2002. (b) Setvín, M.; Aschauer, U.; Scheiber, P.; Li, Y. F.; Hou, W. Y.; Schmid, M.; Selloni, A.; Diebold, U. *Science* **2013**, *341*, 988.

(5) Zhang, M.; Wang, Q.; Chen, C. C.; Zang, L.; Ma, W. H.; Zhao, J. C. *Angew. Chem., Int. Ed.* **2009**, *48*, 6081.

(6) Zhang, K. L.; Liu, C. M.; Huang, F. Q.; Zheng, C.; Wang, W. D. *Appl. Catal. B: Environ.* **2006**, *68*, 125.

(7) Jiang, J.; Zhao, K.; Xiao, X. Y.; Zhang, L. Z. *J. Am. Chem. Soc.* **2012**, *134*, 4473.

(8) Ye, L. Q.; Zan, L.; Tian, L. H.; Peng, T. Y.; Zhang, J. J. *Chem. Commun.* **2011**, *47*, 6951.

(9) (a) Yang, H. G.; Sun, C. H.; Qiao, S. Z.; Zou, J.; Liu, G.; Smith, S. C.; Cheng, H. M.; Lu, G. Q. *Nature* **2008**, *453*, 638. (b) Dean, J. A. *Lange's Handbook of Chemistry*, 15th ed.; McGraw-Hill: New York, 1998.

(10) Sanville, E.; Kenny, S. D.; Smith, R.; Henkelman, G. *J. Comput. Chem.* **2007**, *28*, 899.

(11) (a) Zhao, H. T.; Joseph, J.; Fales, H. M.; Sokoloski, E. A.; Levine, R. L.; Vasquez-Vivar, J.; Kalyanaraman, B. *Proc Natl. Acad. Sci. U.S.A.* **2005**, *102*, 5727. (b) Zhao, H. T.; Joseph, J.; Zhang, H.; Karoui, H.; Kalyanaraman, B. *Free Radical Biol. Med.* **2001**, *3*, 599.

(12) Fukuto, J. M.; Carrington, S. J.; Tantillo, D. J.; Harrison, J. G.; Ignarro, L. J.; Freeman, B. A.; Chen, A.; Wink, D. A. *Chem. Res. Toxicol.* **2012**, *25*, 769.

(13) Emmenegger, L.; King, D. W.; Sigg, L.; Sulzberger, B. *Environ. Sci. Technol.* **1998**, *32*, 2990.

(14) Hirakawa, T.; Nosaka, Y. *Langmuir* **2002**, *18*, 3247.

(15) Jiang, J.; Zhang, L. Z.; Li, H.; He, W. W.; Yin, J. J. *Nanoscale* **2013**, *5*, 10573.

(16) (a) Derrouiche, S.; Loebick, C. Z.; Pfefferle, L. *J. Phys. Chem. C* **2010**, *114*, 3431. (b) Weng, S. X.; Chen, B. B.; Xie, L. Y.; Zheng, Z. Y.; Liu, P. *J. Mater. Chem. A* **2013**, *1*, 3068.